RSC Advances

PAPER

View Article Online
View Journal | View Issue

Cite this: *RSC Adv.*, 2020, **10**, 22387

One-pot preparation of hierarchical Cu_2O hollow spheres for improved visible-light photocatalytic properties†

Yali Dong,[a] Feifei Tao,*[ab] Linxia Wang,*[a] Mingxuan Lan,[a] Jiayan Zhang[a] and Tianjie Hong[a]

As visible light photocatalysts, narrow bandgap semiconductors can effectively convert solar energy to chemical energy, exhibiting potential applications in alleviating energy shortage and environmental pollution. Cu_2O hollow spheres with a narrow band gap and uniform hierarchical structures have been fabricated in a controlled way. The one-pot solvothermal method without any template is simple and facile. The morphologies, crystal structures, composition, specific surface areas, and optical and photoelectric properties of the products were analyzed by various techniques. The hollow and solid Cu_2O spheres could be fabricated by controlling the reaction time, and a possible growth process of the Cu_2O hollow spheres was revealed. The degradation of methyl orange (MO) was used to investigate the visible-light catalytic properties of the Cu_2O samples. More than 90% of MO is degraded under visible light illumination of 20 min, exhibiting a quick catalytic reaction. The rate constant of the Cu_2O hollow spheres was 2.54 times and 46.6 times larger than those of the Cu_2O solid spheres and commercial Cu_2O powder, respectively. The possible photocatalytic mechanism of MO was revealed over Cu_2O hollow spheres through the detection of active species. The as-prepared Cu_2O hollow spheres display improved visible-light catalytic activity and stability, indicating their potential application in wastewater treatment.

Received 17th March 2020
Accepted 27th May 2020

DOI: 10.1039/d0ra02460k

rsc.li/rsc-advances

1. Introduction

Over the years, large-scale architectures of micro- and nano-structured building components with specific morphology have always been of interest to material scientists and chemists.[1–3] In particular, hierarchical and hollow structures have aroused significant attention because of their distinctive functions, novel properties and extensive applications in drug delivery,[4] photonic crystals,[5] catalysis[6] and other areas.[7,8] In comparison with bulk and nanoparticles, the special hollow self-assemblies should be helpful for constructing functional nano-devices and to go deep into the formation of hollow assemblies.

Water sources are becoming increasingly polluted by the rapid expansion of chemical, paper and textile industries, resulting in a global threat to human health.[9,10] Due to the emission of coloured and toxic pollutants from various industrial branches into water bodies, dye compounds as the main pollutant sources in wastewater have caused serious environmental contamination. Therefore, it is very urgent to develop a feasible and inexpensive technology for water treatment. Among a number of chemical and physical methods for wastewater treatment, semiconductor-based photocatalysis displays the rapid and complete mineralization of coloured contaminants.[11–13] Unique semiconductors with tailored electronic structures have high photocatalytic activities and are getting more and more attention, which has been an effective approach for wastewater remediation.[14] However, some wide band gap photocatalysts such as TiO_2 micro- and nano-materials are limited in the solar application for their response under UV light,[15] occupying only about 4% of the whole solar spectrum. Because about 43% of sunlight belongs to visible light, for the purpose of utilizing solar energy efficiently, it is necessary to fabricate narrow band gap photocatalysts with hollow and porous structures to improve photocatalytic activity.

As a p-type semiconductor, cuprous oxide (Cu_2O) with a narrow band gap of about 2.0 eV is of special importance to degrade coloured dyes under sunlight.[16] It is common knowledge that a photocatalytic reaction generally takes place on the surface of the catalyst in close contact with organic pollutants. Thus, the photocatalytic behaviour of Cu_2O largely depends on

[a]*Department of Chemistry and Chemical Engineering, Shaoxing University, Zhejiang 312000, P. R. China. E-mail: feifeitao@usx.edu.cn; wlxsyx@163.com; Tel: +86-575-88342505*

[b]*Shanghai Advanced Research Institute Library, Chinese Academy Sciences, Shanghai 201210, P. R. China*

† Electronic supplementary information (ESI) available. See DOI: 10.1039/d0ra02460k

the morphology, surface structures and specific surface area.[17] Various Cu_2O micro- and nanomaterials, such as nanoparticles, wires, tubes, cubes and octahedrons, have been effectively synthesized in a shape-controlled way.[18–22] Among them, the hierarchical and hollow structures not only have high activities belonging to the nanomaterials, but also have large internal cavities from the hollow structures, facilitating the entry and exit of reactants and products. In addition, the unique hierarchical structures with large sizes can prevent the aggregation of nanoparticles more easily, which contributes to the separation and recycling of the catalyst in practical application.[23–25] Therefore, it is very important to improve the preparation route for hierarchical Cu_2O hollow structures composed of nanoparticles with an intention to enhance the photocatalytic activity.

In this paper, a facile solvothermal approach is proposed to fabricate uniform porous Cu_2O hollow spheres self-assembled by nanocubes with a high specific surface area. Compared with other synthesis methods of Cu_2O hollow spheres,[26,27] our method may not be the best, but it provides another way to construct the Cu_2O hollow self-assembly. In addition, it is a very novel and effective method for synthesizing the hollow materials on a large scale. For obtaining a clear relationship between the special morphology and catalytic properties, the Cu_2O solid spheres have been controllably synthesized for comparison. Meanwhile, the photocatalytic performance of the Cu_2O samples was studied by the degradation of methyl orange (MO), exhibiting high catalytic efficiency and stability under visible light.

2. Experimental section

2.1. Materials

Copper nitrate trihydrate ($Cu(NO_3)_2 \cdot 3H_2O$), 1-butyl-3-methylimidazolium tetrafluoroborate ([BMIM]BF_4), ethylene glycol (EG), methyl orange (MO) and other chemical regents (J&K Chemical, Ltd.) were of analytical grade without further purification. Distilled water was used throughout the experiments.

2.2. Synthesis of Cu_2O samples

In a typical experiment, 0.2416 g of $Cu(NO_3)_2 \cdot 3H_2O$ and 0.2260 g of [BMIM]BF_4 were successively dispersed in 20 mL of EG under vigorous stirring for 24 h. Next, the mixture was transferred and sealed in a Teflon-lined stainless steel autoclave (25 mL capacity), and placed in an oven at 170 °C for 2 h. After the reaction, the obtained product was collected by centrifugation and rinsed at least five times with ethanol and distilled water, and then dried under vacuum at 60 °C for 12 h. The Cu_2O solid spheres were fabricated in a similar way, but the reaction time was only 45 min.

2.3. Characterization

The microstructures and morphologies of the products were investigated by scanning electron microscopy (SEM, JSM-6360LV), transmission electron microscopy (TEM, JEM-1011), and high-resolution transmission electron microscopy (HRTEM, JEM-2100F). The crystal phase of the obtained sample was obtained using X-ray powder diffraction (XRD, Empyrean, Holland PANalytical Company) with Cu Kα radiation source (λ = 0.15406 nm). X-ray photoelectron spectroscopy (XPS) measurements of the obtained samples were performed on a Physical Electronics PHI 1600 ESCA system by an Al Kα X-ray source (E = 1486.6 eV). All binding energies of the constitute elements were referenced to the C 1s peak at 284.6 eV. The Brunauer–Emmett–Teller (BET) surface area and pore size distribution of the samples were measured by nitrogen adsorption on the Empyrean Apparatus (Micromeritics Corp., USA). The optical absorption performance was recorded on a UV-vis diffuse reflectance spectrometer (UV-2550, Shimadzu, Japan) with $BaSO_4$ as a reflectance and a photoluminescence (PL) spectrometer (Fluoromax-3, Horiba Scientific) at room temperature.

The degradation product was analyzed by LC-MS/MS (Triple TOF 5600, AB SCIEX, USA). Separations were obtained by using an Agilent 5 HC-C18 column (250 × 4.6 mm) and the mobile phase composed of 0.1 vol% formic acid aqueous solution and acetonitrile with a flow rate of 0.5 mL min^{-1}. The spectra were acquired in the negative ion scan mode.

2.4. Photoelectrochemical measurements

The photoelectrochemical properties (PEC) of the Cu_2O samples were characterized by cyclic voltammetry and the photocurrent curves on an electrochemical workstation (CHI760E, Chenhua Instruments, Shanghai, China). Generally, in a standard three-electrode cell, a platinum wire was employed as the counter electrode, an Ag/AgCl (saturated KCl) electrode as the reference electrode, and a Cu_2O-modified F-doped tin oxide (FTO) glass as the working electrode, respectively. The FTO glass was cut into 1 cm × 3 cm slices, and successively bathed in a NaOH solution (1.0 mol L^{-1}) for 10 min and acetone for 30 min, respectively. After that, it was washed with water and dried prior to use. 5 mg of the as-prepared powder sample was dispersed ultrasonically in 5 mL of absolute ethanol for 30 min. In addition, 20 μL of the slurry (1 mg mL^{-1}) described above was suspended onto a piece of FTO slice with a fixed active area of 0.196 cm^2 drop by drop. After the FTO slice with electrode film was dried in air at room temperature, it was transferred to an oven at 300 °C for 3 h to construct the Cu_2O-modified FTO working electrode. The photoelectrochemical properties were measured in a Na_2SO_4 aqueous solution (0.5 mol L^{-1}) at 0.6 V (*vs.* Ag/AgCl) under a 250 W xenon arc lamp with a 420 nm cutoff filter.

2.5. Photocatalytic activity

The photocatalytic activities of the catalysts were evaluated by MO decomposition at ambient temperature. In a typical reaction, 10 mg of catalyst powder was dispersed ultrasonically into 50 mL of MO solution (20 mg L^{-1}) in a 100 mL quartz photoreactor with no hydrogen peroxide (H_2O_2). The above suspension was stirred under dark conditions for at least 30 min to reach an adsorption/desorption equilibrium of dye molecules on the photocatalysts. After that, the suspension was exposed to a 250 W xenon arc lamp with a 420 nm cutoff filter (about 100

mW cm^{-2}). The photocatalytic degradation experiments were detected by collecting the suspensions at different irradiation times, which were centrifuged immediately to remove the catalyst particles for analysis. The characteristic absorption intensity of about 465 nm as a monitored parameter on a UV-vis spectrometer was detected to measure the MO concentration.

2.6. Trapping experiments of active species and recycle measurements

To find out the active species, some scavengers were added in the reaction system for quenching tests. *tert*-Butyl alcohol (TBA), benzoquinone (BQ) or disodium ethylenediaminetetraacetate dehydrate (EDTA-2Na) with the same concentration of 1 mmol L^{-1} were used as the scavengers for hydroxide radicals ($\cdot OH$), superoxide radicals ($\cdot O_2^-$) and photogenerated holes (h^+), respectively. The stability tests of the Cu_2O samples were investigated by recycling experiments. The photocatalytic experiments described above were repeated 5 times under the same experimental conditions. After every photocatalytic cycle test, the powder samples were collected by centrifugation and then dried under vacuum for the next test.

3. Results and discussion

3.1. Morphology and crystal structure analysis

The as-obtained sample (by the solvothermal reaction at 170 °C for 2 h) was investigated by SEM and TEM observations (Fig. 1 and S1†). In Fig. 1a, the as-prepared sample shows a uniform sphere-like morphology with diameters ranging from 400 nm to 600 nm. It hardly had any impurity, indicating a high yield and purity. It was obviously observed from some damaged spheres that the as-prepared sample has a hollow structure, which is further proved by the TEM characterization shown in Fig. 1b and S1.† The strong contrast between the dark edge and the pale center was evidence of the hollow nature of the spheres (Fig. S1†). Further observation showed that the hollow spheres have rough surfaces with cubic convex structures. The spherical shell with a thickness of about 80 nm was constructed randomly by a large amount of nanocubes, thereby forming the hollow hierarchical structures. Based on the lattice fringes from the HRTEM image (Fig. 1c) of the hollow spheres, the clear lattice fringes were measured as 0.246 nm. This corresponded to the (111) crystal planes of Cu_2O, further confirming the good crystallization.

The XRD pattern of the as-prepared hollow spheres is displayed in Fig. 1d. According to the Cu_2O standard card (JCPDS no. 78-2076), the diffraction peaks at about 29.5°, 36.4°, 42.3°, 52.5°, 61.4°, 73.5° and 77.4° can be indexed to the crystal planes of (110), (111), (200), (211), (220), (311) and (222) of the primitive cubic crystalline Cu_2O, respectively. According to the line width analysis of the (111) diffraction peak based on the Scherrer formula, an average crystallite size of about 18.7 nm was estimated, which is basically consistent with the particle size observed in the TEM images (Fig. 1b and S1c†). It was considered that the presence of the (111) crystal planes could make Cu_2O a stable photocatalyst.[28]

In order to further verify the composite and the valence states of the elements, the hierarchical hollow spheres were

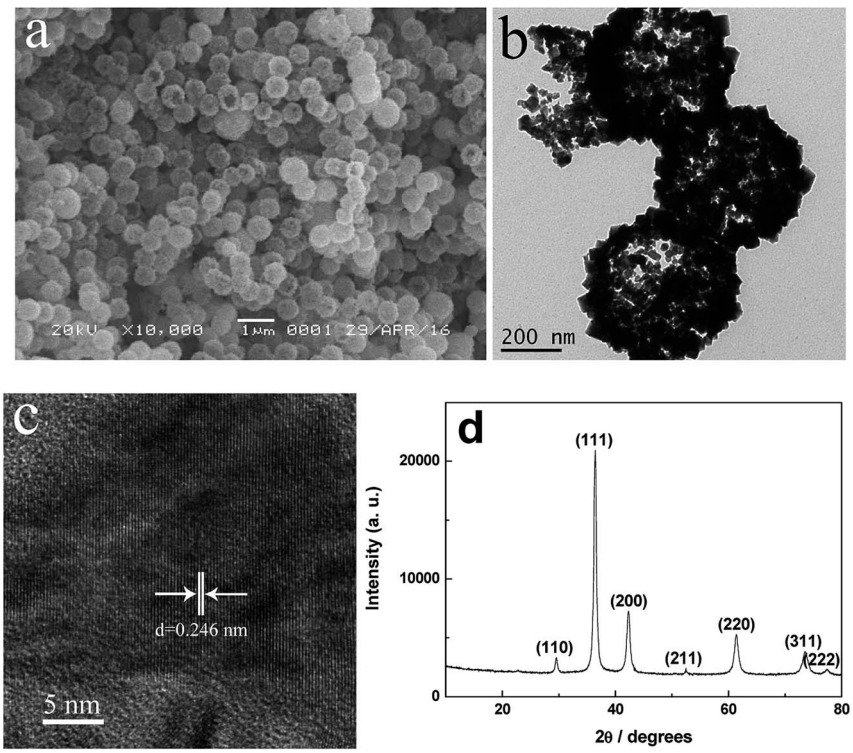

Fig. 1 SEM (a), TEM (b), HRTEM images (c) and XRD pattern (d) of the as-prepared products.

further investigated by XPS. Fig. S2a† shows the XPS survey spectrum of the as-prepared hollow spheres, demonstrating the existence of Cu, O and a trace amount of C elements in the sample. The peaks of the C element might belong to adventitious hydrocarbon in the XPS instrument. Fig. S2b† displays the high-resolution XPS spectra of Cu 2p for the sample. The main peaks at 932.4 and 952.2 eV corresponded to the binding energies of Cu $2p_{3/2}$ and Cu $2p_{1/2}$, respectively, which were readily assigned to either Cu(0) or Cu(I) species.[29] The two peaks located at 934.6 and 954.4 eV and the shake-up satellite peaks at 940–945 eV could be attributed to Cu^{2+}, suggesting the presence of CuO.[29–32] The copper species were further distinguished by the Auger Cu LMM spectrum (Fig. S2c†). The use of the Auger parameter (AP), given by the general equation (eqn (1)), could offer a viable means for exploring the electronic properties of the copper metal.[33]

$$\alpha'_{Cu} = E_k(L_3M_{45}M_{45};\ ^1G) + E_b\left(2p_{3/2}\right) \quad (1)$$

where E_k is the kinetic energy of the $L_3M_{45}M_{45}$; ^1G and E_b is the binding energy of the $2p_{3/2}$ electron. According to Fig. S2b and c,† E_b is 932.4 eV and E_k is 916.2 and 918.4 eV, respectively, and α'_{Cu} is 1848.6 eV for Cu_2O and 1850.8 eV for Cu.[33] So, the peaks located at 570.4 and 568.2 eV could be ascribed to Cu(I) and Cu(0),[31–34] respectively, indicating the existence of Cu_2O and Cu reduced by ionic liquid in the sample. In addition, a small amount of CuO and Cu could not be detected by XRD.

The EDS results of the bulk and surfaces of the hollow spheres (Fig. S3†) showed that the as-prepared products were composed of Cu and O elements, consistent with the XRD and XPS results. Based on the comparison of the content of Cu and O elements (inset in Fig. S3†), it was found that more copper was distributed on the surface of the hollow spheres, which may be due to the fact that the exposed copper on the surfaces of the spheres was easy to be reduced by ionic liquid. The atom ratio of the Cu to O element on the surface of the hollow spheres was 2.37 : 1, which was much higher than the theoretical ratio value of Cu to O element in Cu_2O and CuO, further indicating the existence of Cu(0) on the surface of the sample.

3.2. Growth mechanism

The time-dependent experiments were used to make clear the formation of the Cu_2O hollow spheres by SEM and TEM characterization. Fig. 2 clearly displays the evolution process. At the beginning reaction of 45 min, the as-obtained crystals assembled together to construct the loose solid aggregates with a diameter of approximately 350 nm (Fig. 2a). The solid spheres were clearly seen by TEM (Fig. 2d). As the reaction proceeded to 60 min, the aggregates had a slight increase in size and displayed better uniformity (Fig. 2b). In addition, it was found that the spherical wall was in good condition, while the sphere was gradually dissolved from the outer part to the inner part of the spheres (Fig. 2e). This phenomenon was further strengthened based on the observation of the bright part near the inside of the sphere shell at the reaction time of 90 min (Fig. 2c and f). At the same time, the spheres with the similar size had the rougher surface, and the cubic convex structures could be clearly found in Fig. 2f. According to the X-ray line broadening analysis of the (111) diffraction peaks (Fig. S4†) *via* the Scherrer formula, the Cu_2O samples had an average size of 15.8, 16.2 and 17.5 nm at the reaction times of 45, 60 and 90 min, respectively, which were smaller than that of the Cu_2O hollow spheres. After a reaction time of 2 h, the uniform hollow spherical self-assembly constructed by nanocubes was finally formed, as shown in Fig. 1a and b.

The shape-evolution process of the as-prepared hierarchical Cu_2O hollow spheres with increasing reaction time is a dissolution–recrystallization process. The Ostwald ripening process, where crystallites grow at the expense of the smaller ones, can be used as the underlying mechanism to explain the hollowing process.[35] As shown in Scheme 1, during the ripening process, a large number of nuclei are first formed in a short amount of time. With the reaction progressing, a slow crystal growth triggers the formation of solid spheres, which might last for several minutes. After that, the interior of the solid spheres is gradually dissolved due to the higher surface energies. Based on further reaction with the remaining ions in the solution, the spherical shell becomes rougher and rougher. At the same time, the rough hierarchical surface hinders further dissolution of the spherical shell and promotes the migration of the inner core to the outside driven by high energy. At last, the Cu_2O hollow spheres are observed with the hierarchical shells constructed by nanocubes (Fig. 1a and b). The solid and hollow spheres can be selectively fabricated by controlling the reaction time.

In addition, the effects of other experimental parameters on the morphology evolution were investigated in detail. The reaction temperature has an important impact on the formation of the Cu_2O hollow spheres (Fig. S5†). When it rose to 150 °C, the Cu_2O hollow spheres of about 300 nm with a coarse surface could be observed (Fig. S5a and d†). At the reaction temperature of 160 °C, the hierarchical Cu_2O hollow spheres grew in size and shell thickness with a diameter of about 400 nm and a shell of 50 nm (Fig. S3b and e†). With the reaction temperature up to 170 °C, the hollow spheres developed in size, and the hollow and porous spheres were formed (Fig. 1a and b). At the temperature of 180 °C, the uniformity and integrity of the Cu_2O hollow spheres were destroyed. A large amount of irregular particles could be observed in Fig. S5c and f.† So, at the reaction temperature above 170 °C, the hollow structures became unstable and the sphere shell collapsed into separated particles (Fig. S5f†). Based on the above experiments, the dissolution–recrystallization process that is essential for the preparation of a hollow self-assembly can only take place in the temperature range from 150 to 170 °C. It is very important for the size and shell thickness of the hollow spheres to be adjusted by controlling the reaction temperature.

Apart from the reaction temperature, the $[BMIM]BF_4$ concentration also has a significant effect on the as-prepared Cu_2O products (Fig. S6†). Without $[BMIM]BF_4$, no product was collected. At the $[BMIM]BF_4$ concentration of 0.0125 mol L^{-1}, only irregular nanoparticles were found, as shown in Fig. S6a and f.† With increasing $[BMIM]BF_4$ concentration, the spherical particles gradually grew in size and uniformity, as shown in the SEM images of Fig. S6b–d.† The corresponding TEM images

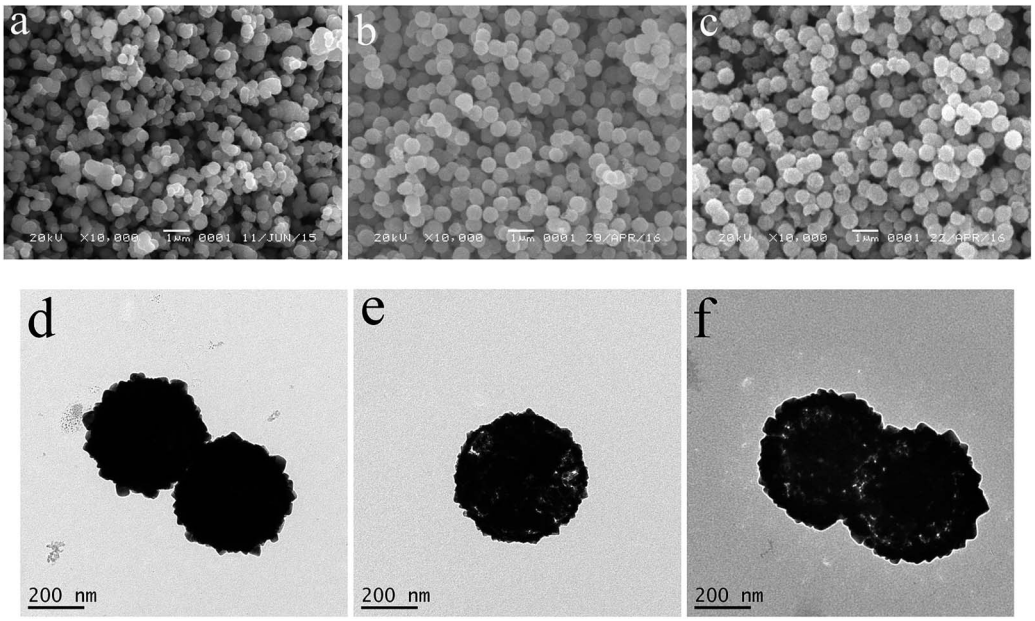

Fig. 2 SEM (a–c) and TEM (d–f) images of the as-prepared products at the different reaction times, (a and d) 45 min, (b and e) 60 min, and (c and f) 90 min.

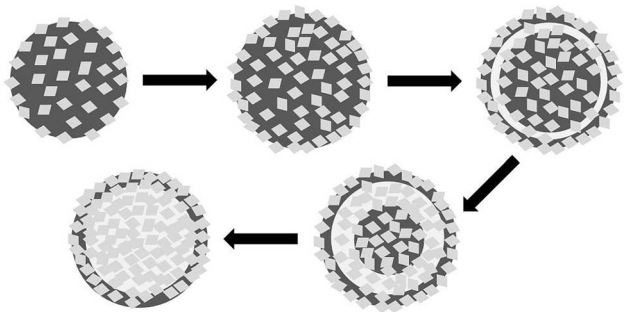

Scheme 1 Formation process of the hierarchical Cu_2O hollow spheres.

further proved the above phenomena and the nanoparticles gradually became empty (Fig. S6g–i†). When the $[BMIM]BF_4$ concentration was increased to 0.15 mol L^{-1}, the sphere size was not consistent and the solid microspheres were found (Fig. S6e and j†). The addition of ionic liquid could lead to the interaction between the Cu^{2+} ion and $[BMIM]BF_4$, which played a significant role in the growth and nucleation rates of the nanocrystals, resulting in the formation of various micro- and nano-crystals.

3.3. Nitrogen adsorption–desorption isotherms

The porous and hollow Cu_2O self-assembly was clearly characterized by SEM and TEM, and further investigated by the N_2 adsorption–desorption isotherms and pore size distribution (Fig. 3a). In order to demonstrate the increased specific surface of the as-prepared hollow spheres due to the hollow and porous structures, the Cu_2O solid spheres (Fig. 2a and d) were fabricated at the reaction time of 45 min and used as a reference. The BET specific surface areas were 21.83 and 14.88 $m^2\ g^{-1}$ for the Cu_2O hollow spheres and solid spheres, respectively. The Cu_2O hollow spheres and solid spheres both displayed type IV isotherms, which are characteristic of most mesoporous materials. The hysteresis loop at the low relative pressure (P/P_0) from 0.4 to 0.9 might be attributed to the mesoporous structures in the interleaving nanocubes or cavities of the hollow spheres, and the hysteresis loop at P/P_0 of 0.9 to 1 might be attributed to the inter-nanoparticle space. The mesopore filling, monolayer coverage and accumulation of particles might lead to the porous structures of the sample, which were further confirmed by the pore size distribution from the Barrett–Joyner–Halenda (BJH) method (inset of Fig. 3). In a very wide range, the pore diameters of the Cu_2O hollow spheres were mainly divided into two categories. One was the mesopore at about 2.9 nm from the surface structure of the sample itself; the other was the micropore from the disordered aggregation of nanocubes in the range of 20–150 nm. For the Cu_2O solid spheres, the corresponding pore size distributions were mainly centered at about 2.2, 32.6 and 125.6 nm due to the existence of mesopores and the aggregation of nanoparticles. Although the Cu_2O solid spheres had smaller pore sizes, the Cu_2O hollow spheres had far more pores than solid ones, resulting in a higher specific surface area. The porous properties of the hollow Cu_2O spheres would increase the specific surface area of the samples, indicating that more reaction sites could be provided and their photocatalytic activities would be improved.

3.4. UV-vis diffuse reflection spectra

The strong absorption in the region of 200–700 nm was observed from the UV-vis spectra of the hollow and solid Cu_2O spheres, indicating the bandgap transition, not from the

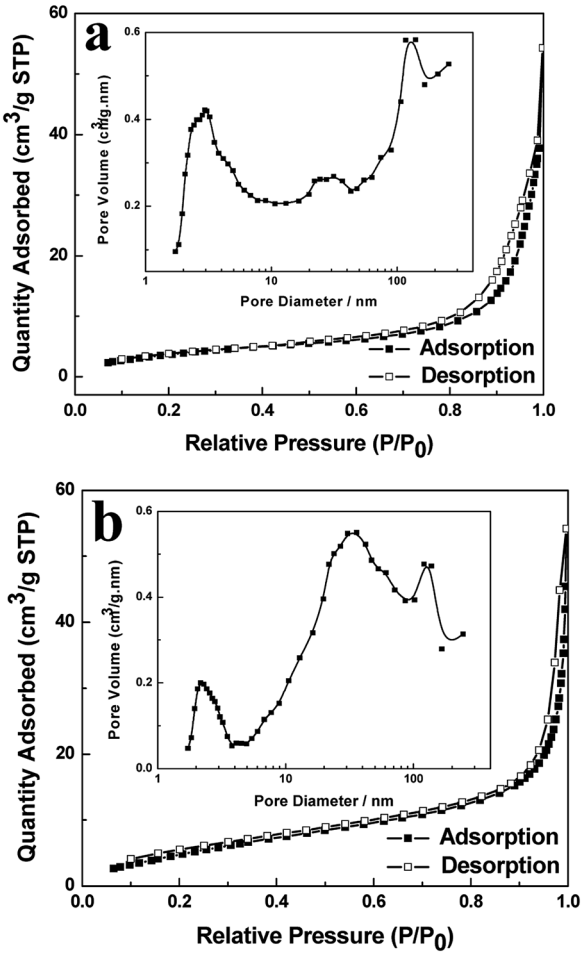

Fig. 3 N_2 adsorption–desorption isotherms and pore size distribution (inset) of the hierarchical Cu_2O hollow spheres (a) and solid spheres (b).

impurity levels (Fig. 4). The absorption edges of the hollow and solid Cu_2O spheres were about 627 nm and 617 nm, respectively. The corresponding bandgap energies (inset of Fig. 4) of the hollow and solid Cu_2O spheres were calculated at about 1.98 and 2.01 eV, respectively, which were identical. Compared with the solid spheres, the hierarchical Cu_2O hollow spheres with special morphology had little effect on the bandgap. In addition, the Cu_2O samples were conductive to efficiently utilize the solar energy and exhibit the high photocatalytic activity.

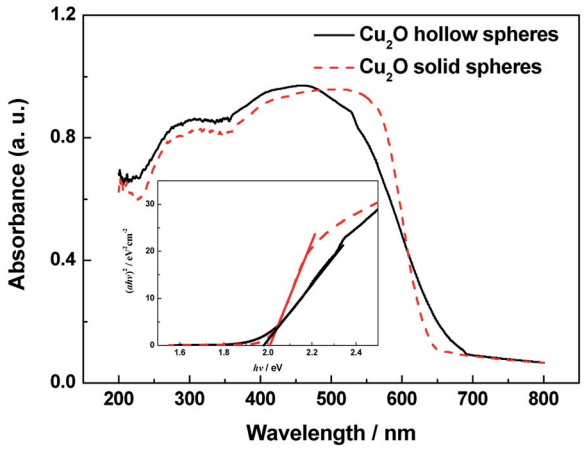

Fig. 4 UV-vis diffuse reflection spectra and $(\alpha h\nu)^2$ *versus* $(h\nu)$ curves (inset) of the hierarchical hollow and solid Cu_2O spheres.

3.5. Photocatalytic properties

Taking the degradation of MO as a model reaction, the photocatalytic activities of the Cu_2O samples were evaluated under visible light. The suspension was magnetically stirred in the dark for at least 30 min before illumination to reach the adsorption–desorption equilibrium. The adsorption capacities of the hierarchical Cu_2O hollow spheres, Cu_2O solid spheres, commercial Cu_2O and Degussa P25 were 32.1%, 18.9%, 0.750% and 0.551%, respectively. The hierarchical Cu_2O hollow spheres exhibited strong adsorption, which can be interpreted by the unique porous and hollow structures.

The UV-vis spectra were measured at regular intervals during the photodegradation of MO over the hierarchical Cu_2O hollow spheres (Fig. 5a). The characteristic peak intensity of MO at about 465 nm decreased with the prolonged irradiation time, indicating that the MO solution was gradually degraded under visible light irradiation. More than 90% of MO was decomposed after 20 min illumination, which exhibited a quick photocatalytic reaction in the presence of the Cu_2O hollow sphere assembly without H_2O_2. For comparison, the similar photocatalytic tests for the solid Cu_2O products, commercial Cu_2O powder and Degussa P25 TiO_2 were conducted under visible light irradiation (Fig. 5b). After a visible light irradiation of 120 min, about 98.5%, 83.5% and 14.0% of the MO solution was degraded for the Cu_2O hollow and solid spheres, and commercial Cu_2O, respectively. The hierarchical Cu_2O hollow spheres showed the highest photocatalytic activities at various irradiation times. However, only about 8.8% of MO was degraded in the presence of P25 and about 3.5% without any photocatalysts, indicating that the Cu_2O photocatalysts were important in the promotion of the photocatalytic reaction of MO.

The MO degradation kinetics was also investigated by the linear simulation of a pseudo first-order Langmuir–Hinshelwood (L–H) mode.[36–38] The L–H model is well established for heterogeneous photocatalysis at low dye concentration, and the kinetic equation (eqn (2)) is shown as follows:

$$r = -\frac{dC}{dt} = K_{app}C \quad (2)$$

where r is the degradation rate, and C_0 and C are the MO concentrations at the adsorption–desorption equilibrium and various intervals of time (t), respectively. K_{app} is the apparent first-order rate constant (min^{-1}), which can be calculated from the gradient of the curve of $\ln(C_0/C)$ *versus* time (t). The K_{app} values in Fig. 5c were estimated to be 0.1138, 0.0448 and 0.00244 min^{-1} for the Cu_2O hollow and solid spheres, and the commercial Cu_2O powder, respectively. The hierarchical Cu_2O hollow spheres showed the largest K_{app} value, which was

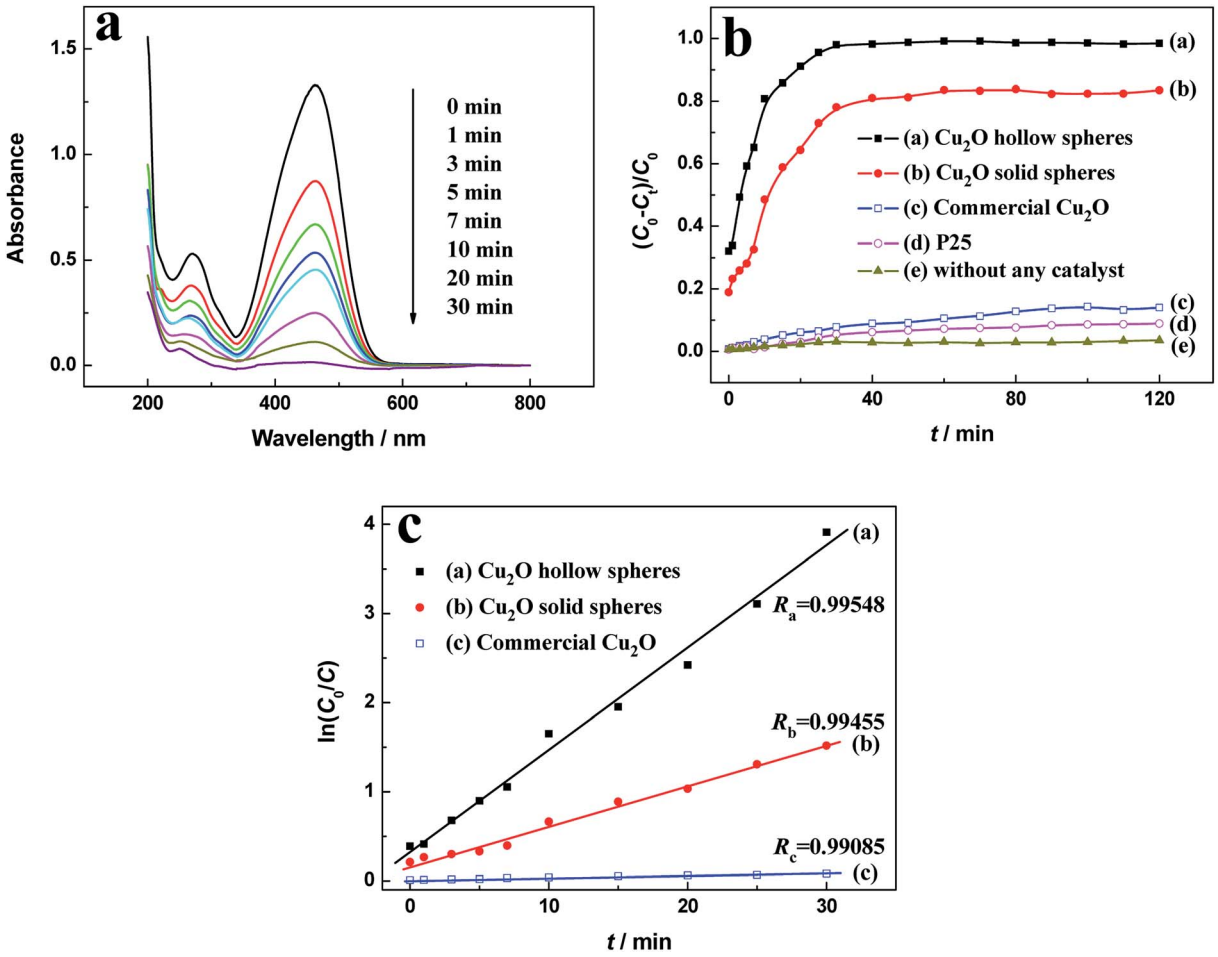

Fig. 5 (a) Absorption spectra of MO solutions for the hierarchical Cu_2O hollow spheres, (b) photodegradation activities and (c) $\ln(C_0/C)$ *versus* *t* curves at the different intervals for various photocatalysts.

approximately 2.54 times and 46.6 times larger than that of the Cu_2O solid spheres and commercial Cu_2O powder. Based on the BET specific surface areas and K_{app} values of the as-prepared Cu_2O samples, the surface area normalised rates (A(surface area)/K_{app}) of MO degradation in the presence of the same amount of photocatalyst (1 mg) were calculated as 5.21 and 3.01 min^{-1} m^{-2} for the hollow and solid Cu_2O spheres, respectively. The results demonstrate that the enhanced photocatalytic activity for the Cu_2O hollow spheres was not only determined by the high specific surface area, but also might be affected by the improved light absorption and doping of a small amount of CuO and Cu.

The photocatalytic activity of the as-prepared Cu_2O hollow spheres was compared to previously reported photocatalysts for the degradation of MO, as shown in Table S1.† Various Cu_2O micro- and nano-materials can effectively degrade MO under their own photocatalytic reaction conditions. Compared with other Cu_2O samples, the as-prepared Cu_2O hollow spheres with the degradation rate as the specific activity of 0.825 mmol g^{-1} h^{-1} displayed satisfactory photocatalytic activity for MO degradation, indicating superior performance in the visible-light photocatalysis.

According to the above experimental results, the hierarchical Cu_2O hollow spheres exhibited excellent catalytic activity for MO degradation, which can be interpreted as follows. First, it is possible that the porous and hollow architectures constructed by nanocubes could provide more active adsorption sites and have full contact with the MO molecules. Second, the existence of a small amount of CuO is helpful for improving the photocatalytic activities due to the efficient separation of photogenerated charges. Finally, a small amount of Cu in the sample can enhance the photocatalytic performance based on the localized surface plasmon resonance (LSPR) effect, referring to the collective oscillation of conductive electrons in metal nanoparticles.[39,40] Thus, as optical antennas or photosensitizers, the plasmonic Cu nanoparticles could be used to enhance the visible-light absorption of photocatalysts through the LSPR effects, so as to improve the photocatalytic reaction rates.[41,42]

To clarify the photocatalytic mechanism of the hierarchical Cu_2O hollow spheres, the active species trapping experiments were performed. The main active species, such as $\cdot OH$, $\cdot O_2^-$ and h^+, are generally detected by TBA, BQ and EDTA-2Na, respectively. As shown in Fig. 6, when TBA was introduced,

the degradation of MO was significantly decreased, indicating that ·OH was a main active species throughout the photodegradation reaction. With the addition of EDTA-2Na, the MO degradation was also obviously suppressed, implying that h^+ had an important impact on the photocatalytic reaction of MO. In addition to TBA and EDTA-2Na, BQ also hindered the MO degradation and $\cdot O_2^-$ was considered to be another active species in the photocatalysis. The reaction between the dissolved O_2 and photo-generated electrons (e^-) could hinder the recombination of photo-generated charges. For a further study on the influence of $\cdot O_2^-$ on the photocatalytic reaction, the photocatalytic degradation of MO over the hierarchical Cu_2O hollow spheres was performed under N_2 atmosphere. Upon bubbling with N_2, the degradation of MO displayed a slight decrease, indicating the relatively minor effect of $\cdot O_2^-$ on the photocatalytic reaction.

After 60 min visible-light irradiation of the MO solution in the Cu_2O hollow spheres, the colorless and transparent solution obtained by centrifugation was taken for LC-MS/MS analysis to identify the products. The mass value (m/z) of the main product detected was 156.996, corresponding to the phenylsulfonic radical,[43] and the obtained chemical structure is shown in Fig. S7,† indicating the incomplete mineralization. Based on the trapping experiments, the hydroxyl and superoxide radicals as the reactive species can attack a more labile oxidation azo (–N=N–) group to break the dye molecules and decolourize the solutions. Subsequently, the benzene ring and branched chains would be broken under the continual attacks of the radical species.[44] However, the oxidation reactions of the intermediates are very complex and the reaction mechanism is not clear.

The possible photocatalytic process of MO over Cu_2O hollow spheres is drawn in Scheme 2. Accordingly, the reported conduction band (CB) (−0.28 V *vs.* NHE) and valence band (VB) (+1.92 V *vs.* NHE) of Cu_2O is more negative than those (+0.46 and +2.16 V *vs.* NHE for CB and VB) of CuO.[31] When irradiated by the visible light, the activated photo-generated electrons transfer from the CB of Cu_2O to that of CuO, and the holes simultaneously migrate from the VB of CuO to that of Cu_2O. So,

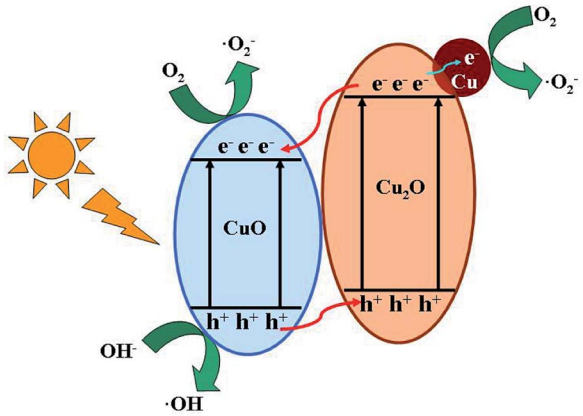

Scheme 2 Photocatalytic reaction mechanism for the hierarchical Cu_2O hollow spheres.

based on the well-matched band structure, a desired heterojunction between Cu_2O and CuO can be established, leading to an improved separation and transfer of photo-generated electrons and holes. In particular, CuO and Cu_2O can serve as different active sites for electron reduction and hole oxidation. Furthermore, the photo-generated electrons on the CB of CuO can reduce O_2 into $\cdot O_2^-$ for the MO degradation. Moreover, with excellent conductivity as good electron acceptors, Cu also accepts the photoexcited electrons from the CB of Cu_2O to produce $\cdot O_2^-$. At the same time, the CuO with the more positive VB potential may be capable of oxidizing hydroxyl groups into ·OH radicals ($E_{\cdot OH/OH^-}$ = +1.99 V, *vs.* NEH) for the enhanced photocatalytic activity.[45] The ·OH radicals can also be generated from the $\cdot O_2^-$ radicals by a photochemical reaction.[46] So, the Cu_2O hollow spheres with a small amount of CuO and Cu can effectively improve the photocatalytic properties.

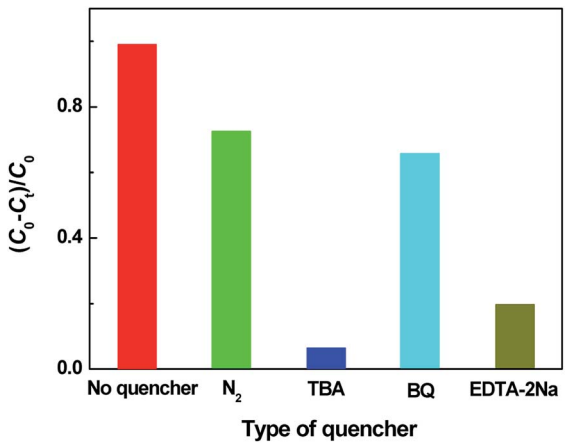

Fig. 6 Effect of a series of quenchers on the degradation of MO over the hierarchical Cu_2O hollow spheres.

3.6. Photoelectrochemical measurements

The separation efficiency of photo-generated charges plays a vital role in improving catalytic activities. The photocurrent comes from the photo-generated electrons transferred from VB to CB excited by light. Therefore, the higher photocurrent suggests the larger separation efficiency of photo-generated charges and better photocatalytic activity. The photocurrent curves for the hollow and solid Cu_2O spheres with chopped illumination are shown in Fig. 7. The photocurrent densities sharply rise to a stable value in the light-on state, but quickly fall to zero in the light-off state. The phenomena suggest that the photo-generated electrons could migrate to the electrode substrate under visible light irradiation to produce a photocurrent. The hierarchical Cu_2O hollow spheres displayed a stronger photocurrent response than the Cu_2O solid spheres. The photocurrent density of the hierarchical Cu_2O hollow spheres with a stable intensity was about 4.6 times higher than that of the Cu_2O solid spheres. This obvious photocurrent enhancement indicated that for the hierarchical Cu_2O hollow spheres, the separation of the photo-generated charges was more effective, which helped to improve its catalytic activity. In addition,

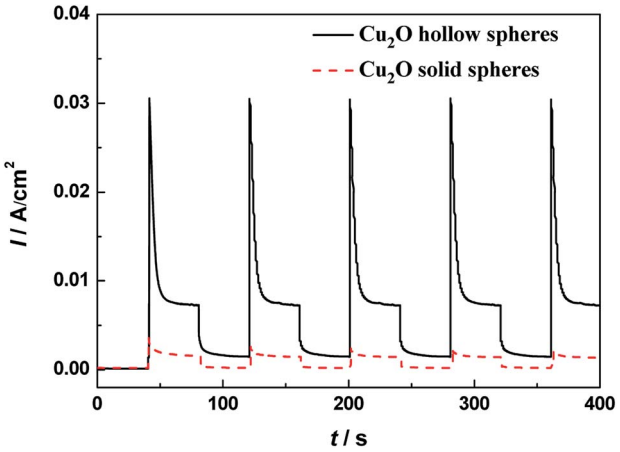

Fig. 7 Transient photocurrent responses of the hierarchical Cu_2O hollow spheres and Cu_2O solid spheres under visible light illumination.

the PL spectra of the Cu_2O samples were measured to reveal the process of migration, transfer and recombination of photo-generated charges in a semiconductor. As shown in Fig. S8,† a strong emission peak of the Cu_2O samples was observed at about 650 nm, indicating the direct recombination of the electrons and holes. The Cu_2O hollow spheres exhibited a lower emission intensity than the Cu_2O solid spheres, indicating the efficient separation of the photo-generated charges.

3.7. Regeneration and reusability

It is important for practical application to study the reproducibility and stability of a photocatalyst throughout the catalytic reaction. In order to assess the regeneration and reusability, the recycling tests of the as-prepared Cu_2O samples were performed to observe the MO degradation under visible light (Fig. 8). For each test, the used photocatalysts were collected by centrifugation, washed with deionized water and dried in air. The MO degradation decreased by 0.46% and 3.5% after five consecutive

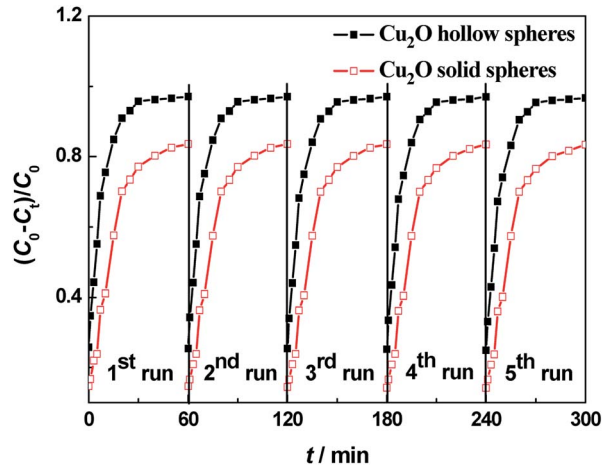

Fig. 8 Recycling experiments of the visible-light photodegradation of MO over hierarchical Cu_2O hollow spheres (solid black squares) and solid Cu_2O spheres (hollow red squares).

experiments for the hollow and solid Cu_2O spheres, respectively. The photocatalytic activities showed almost no decrease for the hierarchical Cu_2O hollow spheres, indicating that the unique porous hollow assembly and the doping of a small amount of CuO and Cu were helpful for the recovery and reuse of the photocatalysts. Due to the existence of many deep and capacious pores, the Cu_2O sample could make full contact with the dye molecules, resulting in the improvement of the photocatalytic activities. So, the hierarchical Cu_2O hollow spheres displayed excellent photocatalytic stabilities and a prominent photocatalytic application.

4. Conclusions

Uniform hierarchical Cu_2O hollow spheres assembled by nanocubes were successfully fabricated on a large scale by the one-step solvothermal approach. Based on the time-dependent experiments, a possible mechanism was proposed to reveal the formation of the hierarchical Cu_2O hollow spheres. Moreover, in comparison with the solid Cu_2O spheres and commercial Cu_2O powder, the hierarchical Cu_2O hollow spheres displayed remarkable visible-light catalytic properties and stability toward MO degradation, which may be due to their distinctive morphology and the doping of a small amount of CuO and Cu. With these unique structures and composition, the hierarchical Cu_2O hollow spheres could be considered an excellent platform, which can significantly enhance the visible-light catalytic performance and open up an approach for wastewater treatment.

Conflicts of interest

There are no conflicts to declare.

Acknowledgements

This work was supported by the National Natural Science Foundation of China (NSFC, grant No. 51372154 and 20901051), Project of Science Technology Department of Zhejiang Province of China (grant No. 2017C33209) and the Science Foundation of Ministry of Housing and Urban-Rural Development of China (grant No. 2015-K4-003).

References

1 X. Ge, X. Song, Y. Ma, H. Zhou, G. Wang, H. Zhang, Y. Zhang, H. Zhao and P. K. Wong, *J. Mater. Chem. A*, 2016, **35**, 14814–14826.
2 Y. Cui, C. Wei, J. Yang, J. Zhang and W. Zheng, *CrystEngComm*, 2016, **18**, 6245–6253.
3 X. Zhang, S. Zhang, B. Chen, H. Wang, K. Wu, Y. Chen, J. Fan, S. Qi, X. Cui, L. Zhang and J. Wang, *Nanoscale*, 2016, **8**, 431–439.
4 X.-Y. Zhao, Y.-J. Zhu, C. Qi, F. Chen, B.-Q. Lu, J. Zhao and J. Wu, *Chem.–Asian J.*, 2013, **8**, 1313–1320.
5 Y. Liu, C. Li, H. Zhang, X. Fan, Y. Liu and Q. Zhang, *Chem. Eng. J.*, 2015, **259**, 779–786.

6 Y. Zhang, Y. Xu, Y. Zhou, S. Xiang, X. Sheng, Q. Wang and C. Zhang, *New J. Chem.*, 2015, **39**, 9372–9379.
7 J. Qiu, Z. Yang, Q. Li, Y. Li, X. Wu, C. Qi and Q. Qiao, *J. Mater. Chem. A*, 2016, **4**, 13296–13306.
8 G. Chen, Y. Gao and H. Zhang, *RSC Adv.*, 2016, **6**, 30488–30497.
9 X. Li, S. Xiong, J. Li, J. Bai and Y. Qian, *J. Mater. Chem.*, 2012, **22**, 14276–14283.
10 S. Caudo, C. Genovese, S. Perathoner and G. Centi, *Microporous Mesoporous Mater.*, 2008, **107**, 46–57.
11 X. Li, T. Xia, C. Xu, J. Murowchick and X. Chen, *Catal. Today*, 2014, **225**, 64–73.
12 J. Hao, Q. Wang and Z. Zhao, *J. Photochem. Photobiol., A*, 2017, **335**, 94–101.
13 A. Taufik, A. Albert and R. Saleh, *J. Photochem. Photobiol., A*, 2017, **344**, 149–162.
14 J. Jiang, X. Zhang, P. Sun and L. Zhang, *J. Phys. Chem. C*, 2011, **115**, 20555–20564.
15 S. Mondal and D. Basak, *Appl. Surf. Sci.*, 2017, **427**, 814–822.
16 Y.-F. Zhao, Z.-Y. Yang, Y.-X. Zhang, L. Jing, X. Guo, Z. Ke, P. Hu, G. Wang, Y.-M. Yan and K.-N. Sun, *J. Phys. Chem. C*, 2014, **118**, 14238–14245.
17 D. Lang, Q. Xiang, G. Qiu, X. Feng and F. Liu, *Dalton Trans.*, 2014, **43**, 7245–7253.
18 M. Amini, H. Naslhajian, S. M. F. Farnia, H. K. Kang, S. Gautam and K. H. Chae, *New J. Chem.*, 2016, **40**, 5313–5317.
19 X. Feng, C. Guo, L. Mao, J. Ning and Y. Hu, *J. Am. Ceram. Soc.*, 2014, **97**, 811–815.
20 Q. Wang, Y. Jia, M. Wang, W. Qi, Y. Pang, X. Cui, W. Ji and J. Yi, *J. Phys. Chem. C*, 2015, **119**, 22066–22071.
21 L. Tang, Y. Du, C. Kong, S. Sun and Z. Yang, *Phys. Chem. Chem. Phys.*, 2015, **17**, 29479–29482.
22 A. Paolella, R. Brescia, M. Prato, M. Povia, S. Marras, L. D. Trizio, A. Falqui, L. Manna and C. George, *ACS Appl. Mater. Interfaces*, 2013, **5**, 2745–2751.
23 C. Deng, X. Ge, H. Hu, L. Yao, C. Han and D. Zhao, *CrystEngComm*, 2014, **16**, 2738–2745.
24 M.-H. Sun, S.-Z. Huang, L.-H. Chen, Y. Li, X.-Y. Yang, Z.-Y. Yuan and B.-L. Su, *Chem. Soc. Rev.*, 2016, **45**, 3479–3563.
25 X. Li, J. Yu and M. Jaroniec, *Chem. Soc. Rev.*, 2016, **45**, 2603–2636.
26 B. Wang, W. Zhang, Z. Zhang, R. Li, Y. Wu, Z. Hu, X. Wu, C. Guo, G. Cheng and R. Zheng, *RSC Adv.*, 2016, **6**, 103700–103706.
27 X. Ge, H. Hu, C. Deng, Q. Zheng, M. Wang and G. Chen, *Mater. Lett.*, 2015, **141**, 214–216.
28 Z. Zheng, B. Huang, Z. Wang, M. Guo, X. Qin, X. Zhang, P. Wang and Y. Dai, *J. Phys. Chem. C*, 2009, **113**, 14448–14453.
29 W. Zhao and C. Liu, *RSC Adv.*, 2020, **10**, 14550–14555.
30 Y. Deng, L. Tang, G. Zeng, C. Feng, H. Dong, J. Wang, H. Feng, Y. Liu, Y. Zhou and Y. Pang, *Environ. Sci.: Nano*, 2017, **4**, 1494–1511.
31 H. Li, Z. Su, S. Hu and Y. Yan, *Appl. Catal., B*, 2017, **207**, 134–142.
32 P. Liu and E. J. M. Hensen, *J. Am. Chem. Soc.*, 2013, **135**, 14032–14035.
33 G. Moretti, A. Palma, E. Paparazzo and M. Satta, *Surf. Sci.*, 2016, **646**, 298–305.
34 I. Platzman, R. Brener, H. Haick and R. Tannenbaum, *J. Phys. Chem. C*, 2008, **112**, 1101–1108.
35 L. Cao, D. Chen and R. A. Caruso, *Angew. Chem., Int. Ed.*, 2013, **52**, 10986–10991.
36 W. Z. Tang and H. An, *Chemosphere*, 1995, **31**, 4157–4170.
37 I. M. Arabatzis, T. Stergiopoulos, D. Andreeva, S. Kitova, S. G. Neophytides and P. Falaras, *J. Catal.*, 2003, **220**, 127–135.
38 J. Li, D. Luo, C. Yang, S. He, S. Chen, J. Lin, L. Zhu and X. Li, *J. Solid State Chem.*, 2013, **203**, 154–159.
39 X. Li, J. Wen, J. Low, Y. Fang and J. Yu, *Sci. China Mater.*, 2014, **57**, 70–100.
40 X. Li, J. Yu, J. Low, Y. Fang, J. Xiao and X. Chen, *J. Mater. Chem. A*, 2015, **3**, 2485–2534.
41 J. Z. Y. Tan, Y. Femández, D. Liu, M. Maroto-Valer, J. Bian and X. Zhang, *Chem. Phys. Lett.*, 2012, **531**, 149–154.
42 R. Kaur and B. Pal, *Appl. Catal., A*, 2015, **491**, 28–36.
43 C. Baiocchi, M. C. Brussino, E. Pramauro, A. B. Prevot, L. Palmisano and G. Marcì, *Int. J. Mass Spectrom.*, 2002, **214**, 247–256.
44 B. Wang, M. Xu, C. Chi, C. Wang and D. Meng, *J. Adv. Oxid. Technol.*, 2017, **20**(2), 20170021.
45 Q. Wei, Y. Wang, H. Qin, J. Wu, Y. Lu, H. Chi, F. Yang, B. Zhou, H. Yu and J. Liu, *Appl. Catal., B*, 2018, **227**, 132–144.
46 Y. Su, A. Nathan, H. Ma and H. Wang, *RSC Adv.*, 2016, **6**, 78181–78186.

